DOI:
10.1002/mrm.25192

Document Version
Early version, also known as pre-print

Title: 'Direct Signal Control' of the Steady-State response of 3D-FSE sequences

Authors: Shaihan Malik*, Arian Beqiri, Francesco Padormo, Joseph V Hajnal

Running Title: Direct Signal Control for 3D-FSE

Address:

Division of Imaging Sciences and Biomedical Engineering

King's College London

St.Thomas' Hospital

London

SE1 7EH

Key words: Extended Phase Graph; Fast Spin Echo; Turbo Spin Echo; RARE; Parallel Transmission

Abstract

Purpose:

Parallel transmission (PTx) offers spatial control of radiofrequency (RF) fields that can be used to mitigate non-uniformity effects in high-field MRI. In practice the ability to achieve uniform RF fields by static shimming is limited by the typically small number of channels, so tailored RF pulses that mix gradient with RF encoding have been proposed. A complementary approach termed "Direct Signal Control" (DSC) is to dynamically update RF shims throughout a sequence, exploiting interactions between each pulse and the spin system to achieve uniform signal properties from potentially non-uniform fields. This work applied DSC to T2 weighted driven-equilibrium 3D-FSE brain imaging at 3T.

Theory & Methods:

The DSC concept requires an accurate signal model, provided by extending the Spatially-Resolved Extended Phase Graph framework to include the steady-state response of driven-equilibrium sequences. An 8-channel PTx body coil was used for experiments.

Results:

Phantom experiments showed the model to be accurate to within 0.3% (RMS). In-vivo imaging showed over two-fold improvement in signal homogeneity compared with quadrature excitation. Although the non-linear optimization cannot guarantee a global optimum, significantly improved local solutions were found.

Conclusion:

DSC has been demonstrated for 3D-FSE brain imaging at 3T. The concept is generally applicable to higher field strengths and other anatomies.

Introduction

Spatial variability of radiofrequency (RF) fields is a prominent issue for MRI at high static magnetic field strengths (≥3T) for which parallel transmission (PTx) has emerged as a potential solution by introducing a degree of spatial and temporal control of the RF fields. The simplest way in which this control can be applied is to try to create uniform fields by using a suitable linear combination of the available transmit channels. This so-called RF shimming is however limited both as a result of the electrical properties of the sample, which may cause substantial field modulation and by the typically small number of available transmit channels whose spatial sensitivity patterns often do not provide sufficient encoding power on their own. Consequently many researchers have combined RF degrees of freedom with gradient encoding, producing tailored RF pulses whose spatial and/or spectral properties are tailored to an individual subject; for a non-comprehensive set of examples see refs.(1–5). These two approaches may be seen as opposite ends of a spectrum spanning the timescale over which the RF modulation is applied. In the case of RF shimming a field pattern is optimized and then fixed in time, while in the case of tailored RF pulses separate waveforms may be applied on each channel, leading to RF field patterns that are modulated over microsecond or millisecond timescales. On the other hand the process of MR image formation typically takes place over an intermediate timescale, as the received signal depends on interactions between multiple RF pulses and the spin system. Such interactions provide an additional mechanism for controlling the evolution of the system. Rather than seeking to control the uniformity of the RF fields or the magnetization created by an individual pulse, the goal of 'Direct Signal Control' (DSC) is to influence the properties of the measured signals by changing the RF field pattern on a pulse-by-pulse basis (i.e. by applying *dynamic* rather than *static* RF shimming). In order to achieve this a model of the signal formation process is required.

The extended phase graph (EPG) algorithm (6) provides such a model that is particularly useful for sequences with a regular repeating time structure, where echo amplitudes may be computed by tracking the populations of 'dephased' states as they evolve through a sequence. The method has been used extensively to characterize RARE (Rapid Acquisition with Relaxation Enhancement (7), also known as Fast- or Turbo- Spin Echo, FSE/TSE) pulse sequences (6,8–10). In recent work (11) this framework was extended to include spatial variations of pulse flip angle/phase. The resulting Spatially Resolved EPG (SR-EPG) framework was used to demonstrate proof of concept Dynamic Signal Control experiments for 2D-FSE imaging, neglecting relaxation effects.

The focus of this work is to achieve uniform signal properties from 3D-FSE with very long echo trains when the RF fields lack spatial uniformity. 3D-FSE sequences have many more pulses than their 2D equivalents – typical echo train lengths are of the order of 100 – so relaxation must be considered both during and crucially, between echo trains. Both the original EPG framework and the SR-EPG extension are generally used to compute echo amplitudes assuming that magnetization is at thermal equilibrium at the start of each echo train. This is a reasonable model when using single shot acquisitions or long repetition times arising from multi-slice imaging. It is however not appropriate for 3D-FSE imaging since the repetition time between shots is frequently limited in order to achieve reasonable acquisition durations. Indeed in order to avoid saturation effects it is often necessary in this case to use a driven equilibrium approach (12) where an additional

refocusing pulse is included, followed by a flip back pulse designed to return residual transverse magnetisation to the longitudinal axis. Echo amplitudes calculated by starting from equilibrium may be thought of as the transient response of the system, however a steady-state will arise over multiple repetitions. This steady-state will generally be a function of all of the flip angles used in the echo train (including the flip-back pulse), as well as tissue relaxation parameters. In this paper a method for computing the steady-state response is introduced and is used as a model for Direct Signal Control of 3D-FSE with parallel transmission.

Theory

A full introduction to EPG calculations can be found in references (8,13–15); here the discussion will be limited to a brief introduction of notation, which will follow closely from that used in ref (11). The magnetization state can be written as a sum over transverse (F_k) and longitudinal (Z_k) states where subscript *k* represents the level of dephasing of that state. Echoes are generated by the F_0 state (non- dephased transverse magnetization). For FSE with N refocusing pulses we can write the amplitudes of the N echoes compactly as

$$\mathbf{I} = [F_0(1), F_0(2), \ldots F_0(N)] = f(\theta_0, \theta_1, \ldots \theta_N, T_1, T_2)$$
$$= f(\boldsymbol{\theta}, T_1, T_2), \qquad (1)$$

where $F_0(n)$ is the population of the refocused state at the time of the n^{th} echo and θ_i is the flip angle of the i^{th} pulse; θ_i is complex where $\arg(\theta_i)$ corresponds to the phase of the i^{th} pulse. The excitation pulse is given index i=0. T_1 and T_2 are longitudinal and transverse relaxation times and *f* signifies application of an EPG algorithm that calculates the $F_0(n)$ for given $\boldsymbol{\theta}$, T_1 and T_2.

Direct evaluation of steady-state echo amplitudes for multi-shot FSE

A driven equilibrium FSE shot with N imaging echoes consists of an excitation pulse with flip angle θ_0, a set of refocusing pulses $\theta_{1\ldots N+1}$, a flip back pulse θ_{N+2} and finally a recovery period T_{REC}, as shown in Fig.1. Refocusing pulse θ_{N+1} generates an echo that is converted to non-dephased longitudinal magnetization (Z_0) by the flip back pulse. Subsequently, transverse and higher order longitudinal coherences have small populations that further decay during the recovery period due to relaxation and also diffusion (16) which preferentially attenuates higher order states. The Z_0 state on the other hand grows with longitudinal recovery. Sequence timing dictates that only even-numbered longitudinal states significantly contribute signal to the next echo train. The population of Z_0 at the end of the recovery period is typically two orders of magnitude higher than the next largest contributor (Z_2); we therefore assume that the only link between each echo train is via Z_0 and consider all other states as zero after the recovery period. Although the system starts from equilibrium magnetization ($\mathbf{M} = [0\ 0\ M_0]^T$) in the first shot, in subsequent shots the starting longitudinal magnetization will approach a dynamic steady-state value M_0^*. Once a steady-state is reached, the longitudinal magnetization at the time points indicated in Fig.1 can be written as: (A) M_0^*, (B) $M_0^\dagger$, (C) $M_0(1-E_R) + M_0^\dagger E_R$ where $E_R \equiv \exp(-T_{REC}/T_1)$. $M_0^\dagger$ is the longitudinal magnetisation directly after the flip-back pulse; this is in general a function of M_0^*, $\boldsymbol{\theta}$, T_1, T_2 and M_0. Without a simple expression for $M_0^\dagger$ the only way to evaluate M_0^* is by brute force, running a transient simulation including Z_0 recovery for multiple shots until a steady state is reached. This so-called "full transient simulation" is used throughout this work as a gold standard but we now show that under certain conditions a direct approach is possible.

Since we neglect the effect of higher order longitudinal states after the recovery period, we may concentrate here just on Z_0; in the EPG terminology just introduced if $Z_0(0)=M_0^*$ then $Z_0(N+2)=M_0^\dagger$ hence the following equation may be derived from standard EPG relations:

$$Z_0(N+2) = \frac{i}{2}\sin\theta_{N+2}\{F_{-1}(N+1) - F_{-1}^*(N+1)\}e^{-\frac{\tau}{2T_2}} + Z_0(N+1)\cos\theta_{N+2} \qquad (2)$$

where τ is the inter-echo spacing. Equation 2 indicates that $Z_0(N+2)$ is comprised of a contribution from the final echo ($F_{\pm1}(N+1)$) and from pre-existing non-dephased longitudinal magnetisation ($Z_0(N+1)$) that may have been present from the beginning, or could have recovered during the shot. CPMG FSE sequences have the general property that the odd and even numbered states are decoupled such that only odd numbered states can contribute to any observed echo while T_1 recovery of Z_0 during the echo train can only contribute to even-numbered states (see for example ref.(15)). As a result the first term in Eq.2 depends only on linear operations applied to the magnetization at the start of the shot (M_0^*) whereas the second term contains contributions from recovering magnetization and is hence not necessarily linear in M_0^*. We therefore arrive at an expression

$$M_0^\dagger = \lambda(\boldsymbol{\theta},T_1,T_2)\, M_0^* + \Delta(\boldsymbol{\theta},T_1,T_2,M_0,M_0^*). \qquad (3)$$

In order to simplify the problem we assume that the longitudinal magnetization after the shot is comprised only from transverse magnetization returned to the z-axis by the flip-back pulse; i.e. $\Delta=0$. The assumption of 'effectively no recovery' is similar to assumptions used by other authors in related circumstances (17–19) and the effect of this simplification is explored later on. In this case $M_0^\dagger = \lambda M_0^*$ so the longitudinal magnetization at point C in Fig.1 is given by $M_0(1-E_R) + \lambda M_0^* E_R$ and given the cyclic nature of the sequence we equate points A and C to obtain an expression for M_0^*:

$$M_0^*(\boldsymbol{\theta},T_1,T_2) = M_0\frac{1-E_R}{1-\lambda E_R}. \qquad (4)$$

A similar expression was derived in ref. (19) for the simpler scenario of 90° excitation and 180° refocusing pulses; in that case λ simply represents T_2 decay throughout the echo train. In this work λ can be defined more generally as the fraction of the starting longitudinal magnetization that is returned to the z-axis after the shot, and it may be directly determined from a standard transient EPG calculation by evaluating

$$\lambda(\boldsymbol{\theta},T_1,T_2) = \frac{Z_0(N+2)}{Z_0(0)}. \qquad (5)$$

The steady-state echo amplitudes, $\mathbf{I_{SS}}(n)$ may thus be computed as

$$\begin{aligned}\mathbf{I_{SS}} &= f_{SS}(\boldsymbol{\theta},T_1,T_2)\\ &= M_0^*(\boldsymbol{\theta},T_1,T_2)\, f(\boldsymbol{\theta},T_1,T_2),\end{aligned} \qquad (6)$$

where both components can be obtained from the results of a single standard EPG calculation.

SR-EPG and Direct Signal Control optimization

All of the preceding theory can be generalized to include spatial variability of the RF fields (11). The steady-state echo amplitudes may thus be written as

$$\mathbf{I_{SS}}(n,\mathbf{r}) = f_{SS}(\boldsymbol{\theta}(\mathbf{r}),T_1,T_2) \quad (7)$$

where now for clarity, the echo amplitudes are written as a function of both echo number *n* and spatial location **r**. For a parallel transmission system the spatially variable flip angles may be written as linear combinations of contributions from multiple channels (20,21) leading to the expression

$$\boldsymbol{\theta}(\mathbf{r}) = \mathbf{A}\,\boldsymbol{\sigma}(\mathbf{r}). \quad (8)$$

In Eq.8 the flip angles are decomposed into a product between A_{ij}, the nominal flip angle applied on channel *j* for pulse *i*, and $\sigma_j(\mathbf{r})$ the dimensionless transmit sensitivity of channel *j*. Both **A** and $\boldsymbol{\sigma}(\mathbf{r})$ can be complex and $\boldsymbol{\sigma}(\mathbf{r})$ is written as a column vector so that $\boldsymbol{\theta}(\mathbf{r})$ is a single set of pulse amplitudes/phases relevant to spatial location **r**. The goal of Direct Signal Control is to find an optimized set of flip angles **A** that will lead to echo amplitudes that conform to a target $\mathbf{T}(n,\mathbf{r})$ by performing the following minimization:

$$\min_{\mathbf{A}} \left\{ \sum_{n\in \boldsymbol{W}, r\in\boldsymbol{\Omega}} \left(|\mathbf{I_{SS}}(n,\mathbf{r})| - \mathbf{T}(n,\boldsymbol{r})\right)^2 + \eta \sum_{n\in \boldsymbol{W}, r\in\boldsymbol{\Omega}} \left(\frac{\partial}{\partial n} arg\left(\mathbf{I_{SS}}(n,\mathbf{r})\right)\right)^2 + \beta \|\mathbf{A}\|_F^2 \right\} \quad (9)$$

where Ω and W represent subsets of spatial locations and echoes, respectively, to be included in the optimization. The first term aims to minimize the difference between the magnitude of the steady-state echo amplitudes and the (real valued) target echo amplitudes. This is similar in spirit to magnitude least-squares RF shimming (22) and allows more degrees of freedom in the optimisation since the spatial distribution of echo phase is not important (spatial smoothness constraints could be included though if necessary). The second term in the cost function aims to penalize temporal phase oscillations, since these would affect the resulting images. The third term aims to control the RF power (and global SAR); the weighting parameters η and β are empirically determined.

Calculation of appropriate refocusing flip angle trains in the absence of RF inhomogeneity is a well-studied area with many interesting strategies including pseudo-steady-states (PSS) (10), TRAPS (23), hyperechoes (14) and tissue-specific signal modulation (24,25). In this work we seek solutions with spatially uniform signals and assume that an 'ideal' set of flip angles exists as a starting point that would yield desired ideal signal properties in the absence of RF inhomogeneity; this will be referred to as the "base sequence" denoted by $\boldsymbol{\theta}_{\mathbf{base}}$ which is not spatially variable (i.e. $\boldsymbol{\theta}_{\mathbf{base}}(\mathbf{r})$ is the same for all **r**). The actual echo amplitudes $\mathbf{I_{SS}}(n,\mathbf{r})$ will vary spatially in the presence of RF inhomogeneity and the goal is to use dynamic RF shimming to restore the ideal behavior. Therefore the natural target for optimization with Eq.9 is to define $\mathbf{T}(n,\mathbf{r})$ as the echo amplitudes that would result if there were no inhomogeneity, i.e.

$$\mathbf{T}(n,\mathbf{r}) = \mathbf{I_{SS}}(\boldsymbol{\theta}_{\mathbf{base}},T_1,T_2) \quad (10)$$

where T_1 and T_2 are those of an appropriately chosen reference tissue.

'No effective recovery' assumption

While the assumption $\Delta(\boldsymbol{\theta},T_1,T_2,M_0,M_0^*)=0$ does not hold for any general set of refocusing pulses, the existence of the flip-back pulse in the driven equilibrium FSE sequence helps, as can be seen from Eq.2 where we note that the second term $Z_0(N+1)\cos\theta_{N+2}$ corresponds to Δ. If the flip-back pulse θ_{N+2}=-90° (as is usually the case) then Δ=0 irrespective of Z_0(N+1). In general RF inhomogeneity means $\cos\theta_{N+2}$ is likely to be small but finite. Similarly for FSE sequences commonly used for imaging we can expect $Z_0(N+1)$ to be small because the excitation results in purely transverse magnetization and recovery is then impeded by the refocusing pulses. Δ is therefore the product of two small numbers. To illustrate this, simulations were performed for two different sets of refocusing pulses (N=100): (i) 180° pulses (ii) pseudo-steady-state refocusing with echo amplitude $0.5M_0$ (15), for a range of θ_0 and θ_{N+2}. Figure 2 displays the error caused by using Eq.6 to compute $\mathbf{I_{SS}}$ compared with the 'true' steady-state echo amplitudes estimated by full transient simulation over 10 shots. Simulations used echo spacing 4.4ms, TR=2500ms, T_1=3651ms, T_2=1429ms (relevant to cerebrospinal fluid at 3T, (26)). As expected, very low error can be achieved if θ_0=90° with 180° refocusing pulses irrespective of θ_{N+2}. Similarly as predicted by Eq.2 θ_{N+2}=-90° leads to zero error for either set of refocusing angles. For the more general case as Fig. 2b shows for the PSS example, a large range of flip angles lead to below 3% simulation error.

Methods

All imaging was performed on a Philips 3T Achieva MRI system fitted with an eight-channel parallel transmission body coil (2kW available peak power per channel) (27) with an eight-channel receive only head coil used for signal reception. The body coil is configured to have a default 'quadrature' mode that produces a quadrature excitation at the centre of the bore when not loaded. Amplitudes and phases of each channel are thus defined relative to quadrature mode (i.e. a relative drive of amplitude 1.0 and phase 0.0 on each channel represents quadrature mode). For brain imaging the quadrature mode excitation is qualitatively similar in both inhomogeneity pattern and range of achieved B_1^+ to a more standard birdcage device; more detailed data on typical B_1^+ variation in the brain from this coil can be found in ref.(4).

Base sequences for T_2 weighted imaging

The methodology outlined in the theory section is entirely general and could be used to obtain a uniform response for any base sequence. In this work we consider T_2 weighted brain imaging examples at 3T with two base sequences given in Table 1. Both generate 100 imaging echoes and in both cases the angles were fixed after the 6th refocusing pulse as a pseudo-steady-state was assumed to have been reached. The first is a standard PSS sequence designed to yield echo amplitudes of $0.5M_0$. Flip angles were computed with the one-ahead algorithm (15,28); the final refocusing pulse θ_{N+1} was computed using Eq.20 in ref.(15). The second base sequence uses higher flip angles at the start in order to move towards the ideal *static* pseudo-steady-state (SPSS; ref.(10)) which yields the highest possible signal for a given flip angle at the cost of producing large oscillations in the first echoes; to compensate 5 dummy echoes are included to delay data readout until the signal stabilizes.

Table 1

	θ_0	θ_1	θ_2	θ_3	θ_4	θ_5	$\theta_{6\ldots N}$	θ_{N+1}	θ_{N+2}
Base sequence 1	90°	90°	53.1°	43.6°	39.8°	38.3°	37.8°	71.1°	-90°
Base sequence 2	90°	137.1°	81.2°	56.4°	45.6°	40.9°	37.8°	109.4°	-90°

Base sequence flip angles. Both sequences generate 100 imaging echoes; N=100 for sequence 1 but N=105 for sequence 2 since this includes 5 dummy echoes. Pulses 1 to N+1 have a phase offset of 90° to fulfill the CPMG condition, which has not been explicitly written here.

Direct Signal Control optimization

The minimization outlined in Eq.9 was formulated with CSF as the reference tissue (T_1=3651ms, T2=1429ms ref.(26)); CSF was chosen because it often dominates the visual appearance of T_2 brain images and this type of imaging is frequently used to visualize fluid pathology with long T_2. Minimization used the Self Organizing Migrating Algorithm (SOMA, (29,30)) implemented in Matlab (The Mathworks, Natick, MA). SOMA is a stochastic 'leader following' method for non-linear optimization; a population of 40 with 40 migrations was used. Although the optimization could be allowed to vary every flip angle independently, for long echo trains this leads to a substantial number of variables and long computation times. Both base sequences in this study use a constant flip angle for the majority of the scan. In keeping with this the rows in **A** corresponding to pulses 6 to N were represented by a single row in the optimization; in other words the same 'RF shim' was used for pulses 6 to N. In optimising base sequence 1, W={1,…,N}, i.e. echoes 1 to N were included in the cost function however for base sequence 2, W={6,…,N} reflecting the presence of 5 dummy (discarded) echoes; note that regardless of which echoes were included in the cost function, all pulses were included in the optimization. The cost function weighting parameters were set empirically (using L-curve methods) as η=0.2 and $\beta=10^{-3}$ and optimization was constrained so that no refocusing pulses exceeded a nominal flip angle of 180° on any channel (this constrains peak power because pulse durations are fixed).

In order to minimize computation times, efficient methods for evaluating EPG calculations were devised and these are discussed in the Appendix, available online as supplementary material. Since the computational load increases linearly with the number of voxels, the spatial domain Ω was decimated to consist of an array of sparse control points distributed through the 3D region of the calculation (in this case the brain of the subject), similar to the approach used in ref.(11). In pilot work (data not shown) it was found that tetrahedral lattices with spacing 25mm allow the whole brain to be characterized by approximately 75 control points with little loss in performance. Further acceleration was achieved by using the Matlab parallel computing toolbox on a Dell Precision T5600 Workstation with 12 cores used simultaneously. Using all of these methods together, the DSC optimization could be performed in approximately 6 minutes.

Data acquisition

The proposed methodology has been tested on phantoms and in-vivo. In this article we present results using both base sequences on a healthy volunteer, who gave written informed consent prior to enrolment, as well as phantom data used for validation. 3D RF field maps were acquired using a two-stage method. First a quantitative B_1^+ map was obtained for the coil's quadrature mode using the AFI sequence (31) with modified spoiling (32) nominal flip angle 80°, TR=30ms/150ms and acquired voxel size 5x5x5mm^3 giving scan duration 4m40s. Next a series of eight low flip angle spoiled gradient echo (SPGR) scans was acquired using the same resolution and field of view but with TR=10ms and nominal flip angle 1° (total duration 2m04s). Relative transmit sensitivity was obtained by dividing each SPGR scan by the sum of all SPGRs and overall B_1^+ was obtained by scaling with the quantitative B_1^+ map; a similar method was used in refs (33,34). Dimensionless transmit sensitivity ($\sigma(\mathbf{r})$) was then obtained by dividing measured B_1^+ by the nominal value. Sensitivity maps were actually obtained for linear combinations of the transmit channels (35) which were inverted to obtain per channel maps. The brain was automatically segmented by applying the FSL brain extraction tool to the SPGR image data; this was used as a mask for the optimizations.

3D-FSE images were obtained using both base sequences using both the quadrature mode of the coil and DSC dynamic shimming. All sequences used TR=2500ms between shots, echo spacing 4.4ms, acquired resolution 1x1x1mm^3 with frequency encoding in the head-foot direction and SENSE reduction factor of 1.7 applied in both phase encoded directions to give total imaging duration of 5m12s for each scan. All RF pulses were non-selective. A hybrid radial-linear phase encoding scheme was used so that each shot filled an approximately radial profile in k_y-k_z with the echo closest to the centre of k-space occurring for the 50th imaging echo. Images were produced directly on the scanner using the standard reconstruction software. An alternative to DSC is to perform static RF shimming in which a single set of channel weights is determined by optimizing for a uniform RF field (as opposed to optimizing directly for uniform echo amplitudes) and applied to all pulses. This method was simulated using the acquired RF sensitivity maps; shimming was performed using magnitude least-squares optimization (22) with varying regularization (equivalent to the third term in Eq.9).

Echo amplitudes resulting from the optimised and quadrature mode flip angles were predicted using a forward model for the entire 3D domain rather than just the decimated grid used for optimization. Though optimization was performed using the direct steady-state method (Eq.6), the solutions were subsequently evaluated using full transient simulations.

A validation experiment was performed with the same 3D FSE sequences using a 10ml sample tube filled with approx. 0.01mM concentration of $MnCl_2$ solution. Frequency encoding was aligned with the long axis of the tube and phase encoding was switched off allowing direct measurement of echo amplitudes. T_1 was measured with multiple inversion recovery experiments as 2292ms. T_2 = 613ms and transmit sensitivity σ=0.95 were determined by fitting calibration data using fixed 180° and 90° refocusing pulses to an EPG model. Note that $\sigma \neq 1$ because of a lack of precision in the scanner's in-built power scaling step.

SAR control and RF safety

The scanner is treated as a normal system when in quadrature mode, and reliable SAR estimates can be obtained. The 3D FSE sequences used in this work have intrinsically low SAR because of their long TRs and low refocusing flip angles. The quadrature mode generic SAR model for an adult male, predicted average

head SAR to be 0.16W/kg and 0.19W/kg respectively for the two base sequences. SAR for the DSC dynamic shimming sequences was estimated by scaling these values with the relative RF power, calculated from $\|\boldsymbol{A}\|_F^2$ (c.f. Eq.9). This estimate does not account for interference between electric fields that may alter the true local SAR. In line with locally adopted rules, a factor of 10 safety margin was included; the relevant regulatory limit is 3.2W/kg for head scanning (36) and scans were thus limited to a predicted SAR of 0.32 W/kg. Preliminary modeling (unpublished data) confirms that this approach respects all relevant regulatory limits and is conservative from a safety point of view.

Results

Figure 3 presents the results of the validation experiment with data showing recorded signals for 10 echo trains, with the first starting from thermal equilibrium. The 'full transient simulation' of 10 cycles of the FSE sequence converges to the same steady state predicted by the direct simulation method. There is also a very good agreement between these simulations and the experimental data for both base sequences; the RMS error is 0.18% for sequence 1 and 0.26% for sequence 2. This excellent agreement suggests that assumptions made in modeling the sequence were reasonable. Note that the experimental data were not fitted to the predictions, rather the global scaling constant was estimated from a calibration scan. Very small differences can most likely be attributed to diffusion effects, which are not included in the simulations (16).

Figure 4 shows in-vivo images as reconstructed by the scanner in the native sagittal plane, all windowed in the same way. All images are free from ghosting artefacts that might indicate unstable echo signals. Both sequences in quadrature mode suffer from B_1 inhomogeneity with low signal at the periphery of the brain, this is particularly true for sequence 1; both images acquired with DSC appear visibly more uniform. Figure 5 shows ratios between images depicted in Fig.4; the images are masked to show brain only and were registered together using the image registration toolkit (37) prior to analysis. Ratios are examined in order to eliminate the effect of the unknown absolute receiver sensitivity profile. Figure 6 is a combination of Figs. 4 and 5 for a coronal section through the same reconstructed images. The coronal images show that as well as low signal in the periphery, in quadrature mode the shading effect is left-right asymmetric for both base sequences. The ratio images are all clearly tissue dependent, with CSF and soft brain tissue changing in different ways. Figs.5a&6e show the ratios of the two quadrature mode images: sequence 1 produces much lower signals in the periphery of the brain and a left-right asymmetry is visible on the coronal section (Seq.1 is more asymmetric than Seq.2 hence the ratio itself is also asymmetric). Although large signal differences exist in the CSF (ratios >1.5) the soft brain tissue also shows spatial signal differences with the ratio Seq.2/Seq.1 approximately 1.3 in peripheral areas. After dynamic shimming the two sequences produce visibly more uniform signal levels through the brain. Examining the ratios of the dynamic shimmed and quadrature images for each base sequence we see that the effect is stronger for Seq.1 (Figs.5c&6g) in which soft tissue signals are boosted by 30-40% in peripheral regions after optimization, and signals are reduced in the centre by up to 20%. The effect is similar but less pronounced for Seq.2 (Figs.5d&6h); here CSF and soft tissues behave slightly differently – CSF signals are boosted in the periphery and remain the same in the centre of the brain however soft tissue signals are around the same in the periphery and are reduced in the centre of the brain.

Finally, the ratios of the two shimmed images (Figs.5b&6f) show little spatial variation, which is consistent with each having substantially achieved the target uniform signal properties.

Figure 7 shows predicted inhomogeneity, measured as normalised root mean square error (NRMSE) with respect to the ideal (σ=1) echo amplitudes, from full transient simulations for Direct Signal Control, quadrature and static RF shimming. The static shimming optimizations were performed with multiple regularization settings penalizing RF power. Inhomogeneity is plotted against predicted head SAR and also maximum flip angle; shaded areas on the graphs show solutions forbidden either because SAR exceeds 0.32W/kg or the maximum nominal flip angle exceeds 180° (peak power constraint). The DSC solutions contain significantly reduced error with little SAR increase, and this cannot be accomplished with static RF shimming.

Figure 8 shows the optimised flip angles and phases for each channel for the two base sequences, along with transmit sensitivities in an axial plane given below (axial planes best reflect the sensitivity variation of the transmit coil used). It is also possible to represent transmit sensitivities in a Fourier basis (e.g. ref.(38)) where the modes are labeled by integer *j* such that a phase increment of $j \times c \times 45°$ is added to channel *c*. Mode 0 corresponds to the quadrature mode of the coil. The flip angles on each channel can also be represented in this domain, such that the overall flip angle is the sum of the Fourier mode sensitivities weighted by the Fourier domain 'flip angles'. In this representation, the base sequences in quadrature mode would have non-zero flip angles only for mode 0; contributions from non-zero modes are an indicator of the contribution of PTx to the solution, since these are not accessible without PTx.

Finally, Fig. 9a shows simulated echo amplitudes for the centre of k-space echo of each sequence for a mid-sagittal plane. Features such as the peripheral image shading and higher signal from base sequence 2 agree qualitatively with Figs.4 and 5a. As illustrated by Figure 2, the direct steady-state simulation method is not exact when $\theta_{N+2} \neq -90°$ which can be the case for the optimized sequences or in the quadrature mode if RF inhomogeneity is present. Figure 9b shows the error compared with the full transient simulation, assumed to be the gold standard. Figure 9c illustrates the proportion of voxels in the 3D domain (the whole brain not just the slice shown) for which this error is less than a given percentage. For quadrature mode 76% and 94% respectively for the two base sequences, have error below 3%. This rises to 97% and 98% for dynamic RF shimmed solutions, respectively.

Discussion & Conclusion

This article explores the use of Direct Signal Control – the direct optimization of image properties via a model, rather than RF field or individual pulse properties - as a means for correcting spatially variable signal and contrast caused by RF inhomogeneity in 3D-FSE imaging, with T_2 weighted brain imaging at 3T used as an example. For the requisite signal model, Spatially Resolved EPGs were extended to allow prediction of a dynamic steady-state formed over multiple TR periods. In-vivo scanning resulted in excellent image quality matching predictions from theory.

In-vivo images were acquired with two base sequences in quadrature mode and then DSC. While both quadrature mode images display shading artefacts due to RF inhomogeneity, these are more prominent for base sequence 1. This is consistent with model predictions in Fig.9a and the error values plotted on Fig.7. The dynamically shimmed images display an obviously more uniform appearance than their quadrature mode equivalents. Noticeable left-right and superior-inferior shading artefacts have been removed; though the latter are more severe the former are perhaps more intrusive since they break anatomical symmetry. Although ratios between shimmed and quadrature images (Figs.5c,d&6g,h) indicate that signals have changed in different ways for the two base sequences, the ratio between the two shimmed images (Figs.5b&6f) is much more uniform in appearance. This is consistent with both shimmed images being more spatially uniform or at least having the same degree of uniformity, and is in keeping with Fig.7 which suggests that although the quadrature mode NRMSE values differ, the NRMSE after dynamic shimming should be approximately the same for both sequences. However as Fig.8 indicates, the optimized pulse amplitudes and phases have not converged to a common solution, instead the separate solutions are more in line with the intended behavior of the respective base sequences. This can be seen from the differing tissue-specific responses visible on the ratios (Figs.5b&6f), for example sequence 2 produces more signal in CSF than sequence 1. The Fourier representation of the optimized flip angles (Figures 8e&f) can help to visualize this by separating the quadrature mode (mode 0) which dominates for this coil configuration as it produces the most B_1^+ field per-unit input power, from higher order modes which add some spatial control and directly reveal the contribution from parallel transmission. The optimized solution for base sequence 1 retains the property of having the same flip angle for excitation and first refocusing pulses (mode 0 remains the same for θ_0 and θ_1) whereas for base sequence 2 θ_1 is much larger than θ_0, as with the unoptimized versions. In both sequence variants significant contributions are made especially from modes +1 and -1 for the first two pulses; these modes allow higher flip angles to be produced at the periphery of the brain. In contrast, static RF shimming uses only these higher order mode contributions to attempt to correct for nonuniformity (i.e. no dynamic modulation). Figure 7 summarises simulations of the expected performance of static shimming when compared with DSC and quadrature excitation. The DSC solutions achieve much lower NRMSE than that which is achievable by static shimming within SAR and peak power limits.

It should however be noted that the SAR values used in this work – derived from the computed values for quadrature excitation, scaled by the RF power relative to quadrature mode – are not necessarily accurate, and the charts in Fig.7a&c are more indicative of average power. For brain imaging at 3T we have found a generally good correspondence between average power and the head average SAR, and it is this value rather than local 10g SAR that is generally the limiting factor. Nevertheless a factor 10 margin of error was introduced for safety evaluation purposes. For situations with larger fields of view and/or higher B_0 field strengths this would no longer be appropriate. In those circumstances predictions from SAR models could be used both to assess safety and also to penalize/constrain solutions by suitably modifying the cost function; such methods are actively under development in the wider field (e.g. (39–41)) and could readily be adopted into the proposed methodology where necessary.

A key aspect of the presented work is that the optimization seeks to control steady-state and not transient echo amplitudes. This is particularly important for optimization of the last two pulses of the pulse train since these

affect signals in subsequent shots (and hence the final steady-state) but they do not contribute to the transient response of the shot in which they are played out. The proposed approach enables the effect of *all* pulses on the observed steady-state echo amplitudes to be evaluated, allowing optimization of all on the same terms. Fig.8 shows that the last two pulses are indeed changed from their starting values by the optimization. The proposed 'direct' estimation of the steady-state is an important means for performing this optimization because it allows fast calculation. The method is based on the assumption that Z_0 at the end of the shot can be expressed as a fraction of the value present just prior to the excitation. The related assumption that Z_0 does not recover during the FSE shot has been used by other authors (17–19) is only truly the case for a 90° excitation pulse and 180° refocusing pulses making it unsuitable for low refocusing angle PSS sequences of the type used. It is the addition of the flip-back pulse in the driven equilibrium variant of the sequence that makes the use of the assumption more generally reasonable. RF inhomogeneity of course means that this condition is violated, and Fig.9b shows the errors in using the direct estimation method. The largest errors occur for base sequence 1 with quadrature excitation, and in this case only 76% of the voxels in the 3D calculation have an error lower than 3%, whereas this figure is above 97% when using dynamic shimming. Although the optimization is not constrained to ensure that θ_{N+2}=-90°, the optimization has a natural tendency to keep this close to -90° so that remaining transverse magnetization is efficiently stored longitudinally. This tends to keep simulation error low, as seen.

DSC relies on a large non-linear optimization (Eq.9); the SOMA method was chosen because of prior experience of good performance however many optimization methods exist. Although convergence to a global optimum for a given target $\mathbf{T}(n,\mathbf{r})$ cannot be guaranteed it should be noted that the starting point - the base sequence – is the operating point that would be used for imaging in normal practice. The present method improves on this by iteratively updating the inputs to the system, so will always drive to a better operating point. Exploring how to ensure that improved performance approaches optimal performance remains a matter for future research. In order to make the method tractable for online optimization many steps were taken to minimize computation time: as well as the direct steady-state calculation just discussed, an approximate method involving dropping large numbers of the states from the calculation was also implemented (see Appendix). Finally, since the SR-EPG simulation for each spatial location is effectively independent, approximately linear improvements in speed can be obtained by reducing the number of control points and by using parallel computation. Using these methods, acceptable computation times for this proof-of-concept study (approx. 6 minutes for 9 flip angles and 8 channels using 75 control points with 12-fold parallel computation) were achieved using Matlab. Online clinical implementation would require acquisition of B_1^+ maps before optimization; much progress has been made by others in accelerating these mapping approaches (for example ref.(42)) and computation times of a few minutes could feasibly be tolerated if run concurrently with other scanning. Further reductions could be achieved by implementing in a more efficient language and by taking advantage of highly parallel graphics processers.

Although the method proposed is general, some of the methodology used in the present study is specific to the example implementation. For example, the base sequences had only 9 independent flip angles (Table 1) and this meant that the optimization could naturally be performed with only 9 unknowns per channel. This

makes for a calculation which is tractable in a limited amount of time, and is not unreasonable for PSS sequences in which the PSS is established by the first few pulses (10). In principle though every pulse could be included independently in the optimization or they could be subdivided in other ways; for example in a TRAPS sequence (23) the ramp of increasing flip angles could be scaled by a common RF shim setting, or in a 'tissue specific' modulation sequence (24,25) the different 'phases' of the signal evolution curve could use different RF settings. Additionally, signals have been optimised for specific "reference tissue" which in this case was actually CSF. In practice the contrast between tissues is also an important consideration. In choosing a single reference tissue with particular properties we expect that similar tissues will behave in a similar way – CSF was selected as the reference tissue in this work so that it could be representative of signals from fluids and tissues with very long T_2. Alternatively it would be possible to use multiple tissue types in the optimisation, or to even specifically optimize the contrast between two tissues (i.e. the difference in predicted echo amplitudes) and this will be left as the subject of future work.

Direct Signal Control via dynamic RF shimming employs interactions between multiple RF pulses to control the evolution of signals throughout a sequence. This is useful because in many circumstances a given transmit coil may not provide sufficient spatial degrees of freedom with which to produce uniform B_1^+ fields using static RF shimming alone. Another way of obtaining additional control is to use 'tailored' RF pulses which contain some degree of gradient encoding (4,43–45). A recent study (46) used a similar approach to reduce inhomogeneity artefacts in T_2 weighted 3D-FSE brain images at 7T. This approach may be viewed as an extension of static RF shimming since it uses a fixed spatial modulation over time. In the present article, short non-selective RF pulses were used throughout. Spatially tailored pulses have the drawback of longer durations leading to larger inter-echo spacings, as well as complicated frequency responses. For the 3T examples in this paper dynamic RF shimming alone gives good results however it is possible that in other situations with more extreme inhomogeneity (such as 7T imaging), some degree of spatial encoding with tailored RF pulses may be desirable; the two approaches are not mutually exclusive. The concept of Direct Signal Control is agnostic to the sub-elements of the sequences used and the SR-EPG framework provides an overarching model to combine these effects; by directly evaluating expected echo amplitudes we can sidestep issues such as explicit phase matching of RF pulses to maintain the CPMG condition and constrain amplitudes of larger angle pulses while being less restrictive with those with smaller angles. This same approach could be taken for designing sequences of tailored RF pulses acting together; interactions could then be used to give additional degrees of freedom that would allow the required spatial encoding (hence duration) of the individual pulses to be reduced.

The concept of Direct Signal Control is to achieve desired image properties by considering the pulse sequence as a whole, rather than by designing the properties of individual pulses. This paper has demonstrated that this approach can be used for 3D-FSE imaging with long pulse trains to produce high quality images with excellent signal uniformity despite operating with non-uniform RF fields and does so by considering not just the action of one pulse or even one train of pulses, but the dynamic equilibrium reached by applying a train multiple times.

Acknowledgements

SJM acknowledges Fellowship support from the Engineering and Physical Sciences Research Council (EPSRC; EP/L00531X/1). The authors also acknowledge project funding from the EPSRC (EP/H046410/1) and the Medical Research Council (strategic funds) and support from the Department of Health via the National Institute for Health Research (NIHR) comprehensive Biomedical Research Centre award to Guy's & St Thomas' NHS Foundation Trust in partnership with King's College London and King's College Hospital NHS Foundation Trust. The Image Registration Toolkit was used under Licence from Ixico Ltd.

References

1. Setsompop K, Alagappan V, Gagoski B, et al. Slice-selective RF pulses for in vivo B1+ inhomogeneity mitigation at 7 tesla using parallel RF excitation with a 16-element coil. Magn. Reson. Med. 2008;60:1422–32.

2. Zelinski AC, Wald LL, Setsompop K, Alagappan V, Gagoski B a, Goyal VK, Adalsteinsson E. Fast slice-selective radio-frequency excitation pulses for mitigating B+1 inhomogeneity in the human brain at 7 Tesla. Magn. Reson. Med. 2008;59:1355–64.

3. Sung K, Nayak KS. B1+ compensation in 3T cardiac imaging using short 2DRF pulses. Magn. Reson. Med. 2008;59:441–6.

4. Malik SJ, Keihaninejad S, Hammers A, Hajnal J V. Tailored excitation in 3D with spiral nonselective (SPINS) RF pulses. Magn. Reson. Med. 2012;67:1303–15.

5. Cloos M a, Boulant N, Luong M, Ferrand G, Giacomini E, Le Bihan D, Amadon a. kT -points: short three-dimensional tailored RF pulses for flip-angle homogenization over an extended volume. Magn. Reson. Med. 2012;67:72–80.

6. Hennig J. Multiecho imaging sequences with low refocusing flip angles. J. Magn. Reson. 1988;407:397–407.

7. Hennig J, Nauerth A, Friedburg H. RARE imaging: a fast imaging method for clinical MR. Magn. Reson. Med. 1986;3:823–33.

8. Scheffler K. A pictorial description of steady-states in rapid magnetic resonance imaging. Concepts Magn. Reson. 1999;11:291–304.

9. Hennig J. Echoes—how to generate, recognize, use or avoid them in MR-imaging sequences. Part II: Echoes in Imaging Sequences. Concepts Magn. Reson. 1991;3:179–192.

10. Alsop D. The sensitivity of low flip angle RARE imaging. Magn. Reson. Med. 1997;37:176–184.

11. Malik SJ, Padormo F, Price AN, Hajnal J V. Spatially resolved extended phase graphs: Modeling and design of multipulse sequences with parallel transmission. Magn. Reson. Med. 2012;68:1481–94.

12. Van Uijen CM, den Boef JH. Driven-equilibrium radiofrequency pulses in NMR imaging. Magn. Reson. Med. 1984;1:502–7.

13. Hennig J. Echoes—how to generate, recognize, use or avoid them in MR-imaging sequences. Part I: Fundamental and not so fundamental properties of spin echoes. Concepts Magn. Reson. 1991;3:125–143.

14. Hennig J, Scheffler K. Hyperechoes. Magn. Reson. Med. 2001;12:6–12.

15. Hennig J, Weigel M, Scheffler K. Calculation of flip angles for echo trains with predefined amplitudes with the extended phase graph (EPG)-algorithm: principles and applications to hyperecho and TRAPS sequences. Magn. Reson. Med. 2004;51:68–80.

16. Weigel M, Schwenk S, Kiselev VG, Scheffler K, Hennig J. Extended phase graphs with anisotropic diffusion. J. Magn. Reson. 2010;205:276–85.

17. Visser F, Zwanenburg JJM, Hoogduin JM, Luijten PR. High-resolution magnetization-prepared 3D-FLAIR imaging at 7.0 Tesla. Magn. Reson. Med. 2010;64:194–202.

18. Wong E, Liu T, Luh W. T1 and T2 selective method for improved SNR in CSF-Attenuated imaging: T2-FLAIR. Magn. Reson. Med. 2001;45:529–532.

19. Busse RF, Riederer SJ, Fletcher JG, Bharucha a E, Brandt KR. Interactive fast spin-echo imaging. Magn. Reson. Med. 2000;44:339–48.

20. Katscher U, Börnert P, Leussler C, van den Brink JS. Transmit SENSE. Magn. Reson. Med. 2003;49:144–50.

21. Zhu Y. Parallel excitation with an array of transmit coils. Magn. Reson. Med. 2004;51:775–84.

22. Setsompop K, Wald LL, Alagappan V, Gagoski B a, Adalsteinsson E. Magnitude least squares optimization for parallel radio frequency excitation design demonstrated at 7 Tesla with eight channels. Magn. Reson. Med. 2008;59:908–15.

23. Hennig J, Weigel M, Scheffler K. Multiecho sequences with variable refocusing flip angles: optimization of signal behavior using smooth transitions between pseudo steady states (TRAPS). Magn. Reson. Med. 2003;49:527–35.

24. Mugler (III) JP, Kiefer B, Brookeman JR. Three-Dimensional T2-Weighted Imaging of the Brain Using Very Long Spin-Echo Trains. Proc ISMRM 2000;8:687.

25. Busse RF, Hariharan H, Vu A, Brittain JH. Fast spin echo sequences with very long echo trains: design of variable refocusing flip angle schedules and generation of clinical T2 contrast. Magn. Reson. Med. 2006;55:1030–7.

26. Weigel M, Hennig J. Contrast behavior and relaxation effects of conventional and hyperecho-turbo spin echo sequences at 1.5 and 3 T. Magn. Reson. Med. 2006;55:826–35.

27. Vernickel P, Röschmann P, Findeklee C, Lüdeke K-M, Leussler C, Overweg J, Katscher U, Grässlin I, Schünemann K. Eight-channel transmit/receive body MRI coil at 3T. Magn. Reson. Med. 2007;58:381–9.

28. Le Roux P, Hinks RS. Stabilization of echo amplitudes in FSE sequences. Magn. Reson. Med. 1993;30:183–90.

29. Zelinka I. SOMA—self-organizing migrating algorithm. In: Onwubolu GC, Babu B V, editors. New optimization techniques in engineering. Springer; 2004. pp. 167–217.

30. Alexander DDC. A general framework for experiment design in diffusion MRI and its application in measuring direct tissue-microstructure features. Magn. Reson. Med. 2008;60:439–48.

31. Yarnykh VL. Actual flip-angle imaging in the pulsed steady state: a method for rapid three-dimensional mapping of the transmitted radiofrequency field. Magn. Reson. Med. 2007;57:192–200.

32. Nehrke K. On the steady-state properties of actual flip angle imaging (AFI). Magn. Reson. Med. 2009;61:84–92.

33. Van de Moortele P-F, Snyder C, DelaBarre L, Adriany G, Vaughan T, Ugurbil K. Calibration Tools for RF Shim at Very High Field with Multiple Element RF Coils : from Ultra Fast Local Relative Phase to Absolute B1+ Mapping. Proc ISMRM 2007;15:1676.

34. Curtis AT, Gilbert KM, Klassen LM, Gati JS, Menon RS. Slice-by-slice B1+ shimming at 7 T. Magn. Reson. Med. 2012;68:1109–16.

35. Malik SJ, Larkman DJ, Hajnal J V. Optimal linear combinations of array elements for B1 mapping. Magn. Reson. Med. 2009;62:902–9.

36. International Electrotechnical Commission (IEC) 60601-2-33 Medical electrical equipment - particular requirements for the safety of magnetic resonance equipment for medical diagnosis.

37. Studholme C, Hill DLG, Hawkes DJ. An overlap invariant entropy measure of 3D medical image alignment. Pattern Recognit. 1999;32:71–86.

38. Alagappan V, Nistler J, Adalsteinsson E, et al. Degenerate mode band-pass birdcage coil for accelerated parallel excitation. Magn. Reson. Med. 2007;57:1148–58.

39. Graesslin I, Homann H, Biederer S, Börnert P, Nehrke K, Vernickel P, Mens G, Harvey P, Katscher U. A specific absorption rate prediction concept for parallel transmission MR. Magn. Reson. Med. 2012;68:1664–74.

40. Eichfelder G, Gebhardt M. Local specific absorption rate control for parallel transmission by virtual observation points. Magn. Reson. Med. 2011;66:1468–76.

41. Zhu Y, Alon L, Deniz CM, Brown R, Sodickson DK. System and SAR characterization in parallel RF transmission. Magn. Reson. Med. 2012;67:1367–78.

42. Nehrke K, Börnert P. DREAM-a novel approach for robust, ultrafast, multislice B(1) mapping. Magn. Reson. Med. 2012;68:1517–26.

43. Pauly J, Nishimura D, Macovski A. A k-space analysis of small-tip-angle excitation. J. Magn. Reson. 1989;81:43–56.

44. Grissom W, Yip C, Zhang Z, Stenger VA, Fessler J a, Noll DC. Spatial domain method for the design of RF pulses in multicoil parallel excitation. Magn. Reson. Med. 2006;56:620–9.

45. Saekho S, Yip C, Noll DC, Boada FE, Stenger VA. Fast-kz three-dimensional tailored radiofrequency pulse for reduced B1 inhomogeneity. Magn. Reson. Med. 2006;55:719–24.

46. Eggenschwiler F, O'Brien KR, Gruetter R, Marques JP. Improving T 2 -weighted imaging at high field through the use of k T -points. Magn. Reson. Med. doi: 10.1002/mrm.24805.

Figure Legends

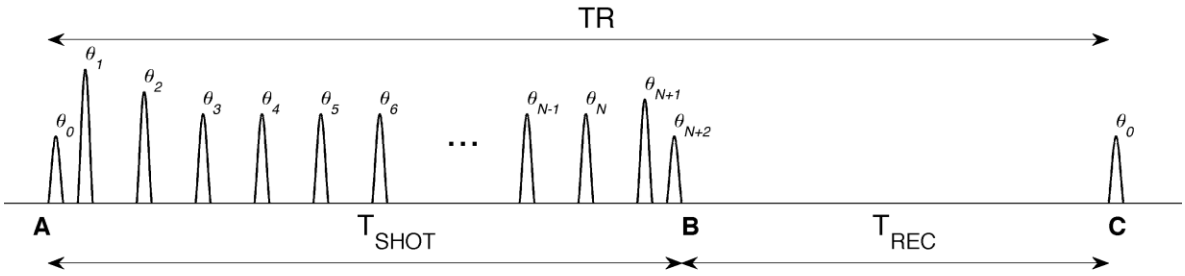

Figure 1 Schematic of multi-shot driven-equilibrium 3D-FSE sequence.

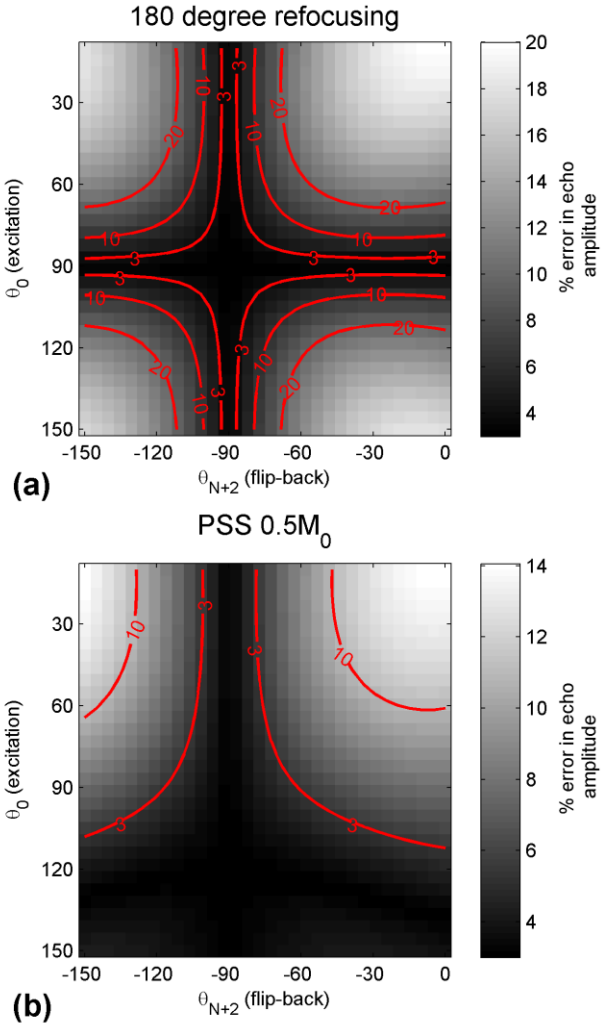

Figure 2 Percentage error in predicted echo amplitudes when calculated using direct estimation method (Eq.6) over a range of excitation (θ_0) and flip-back (θ_{N+2}) pulse angles. (a) 180° refocusing pulses. (b) Variable refocusing angles designed to yield a PSS with echo amplitudes of $0.5M_0$. Contours are drawn for errors of 3%, 10% and 20%.

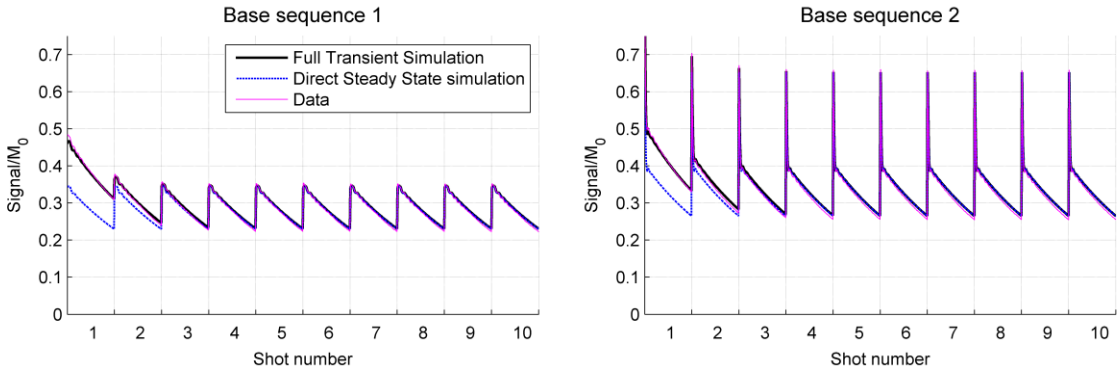

Figure 3 Results of phantom experiments comparing 'full transient simulation', direct computation of steady-state and experiment.

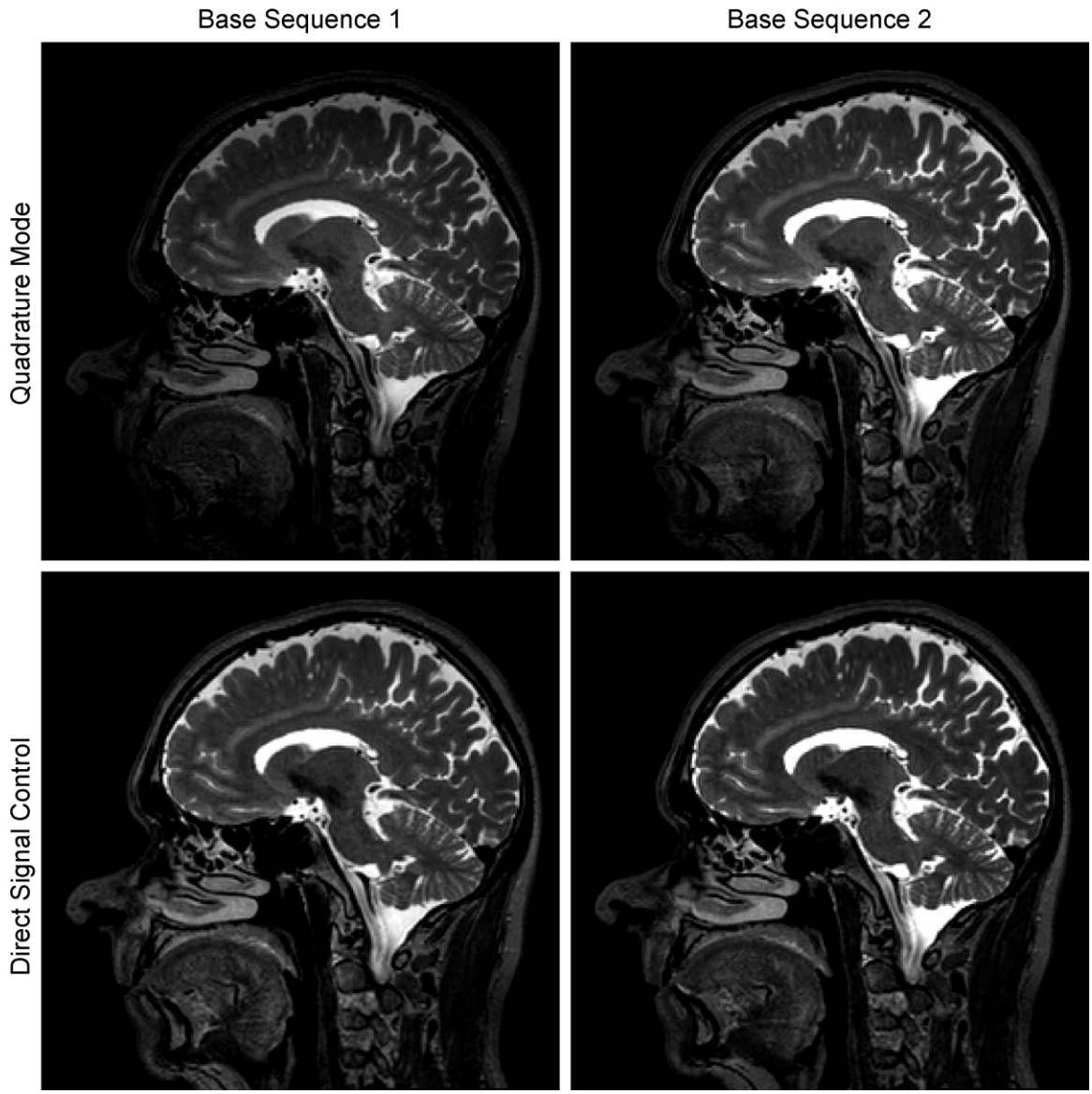

Figure 4 In-vivo images acquired using both base sequences (see Table 1) with quadrature excitation and DSC dynamic shimming.

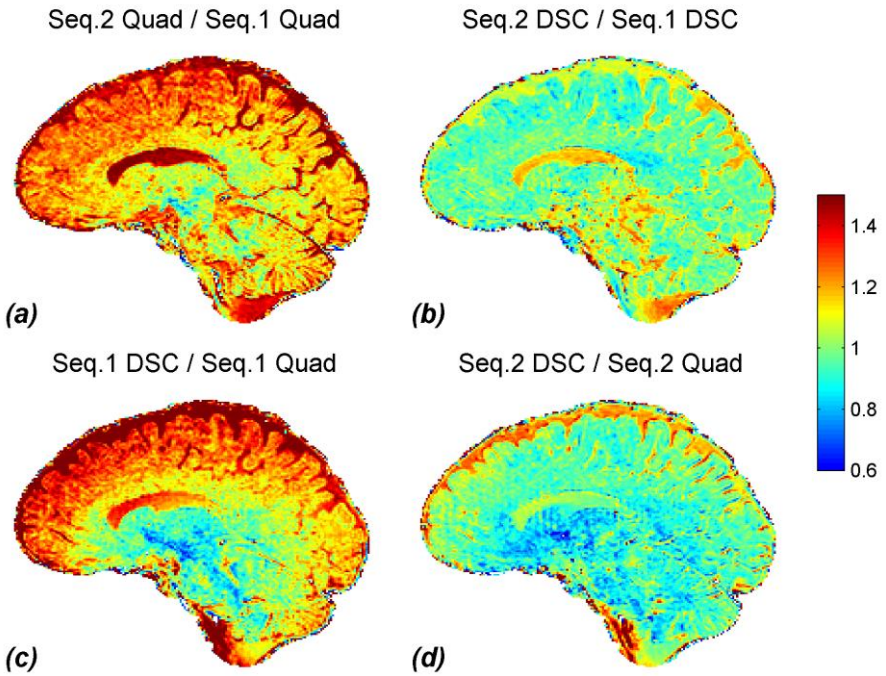

Figure 5 Ratios of acquired images (post registration and brain extraction). (a) Base sequence 2 (BS2) quadrature divided by base sequence 1 (BS1) quadrature. (b) BS2 dynamic shim divided by BS2 dynamic shim. (c) BS1 ratio of dynamic shimmed image to quadrature image. (d) BS2 ratio of dynamic shimmed image to quadrature image.

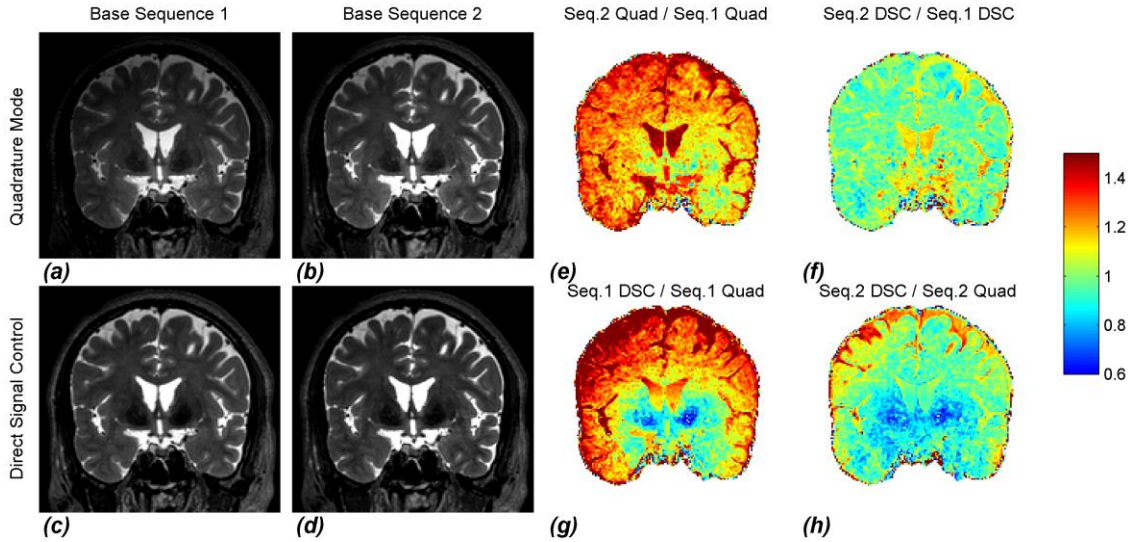

Figure 6 Combined Figures 4 and 5 for coronal reformat through the same 3D data.

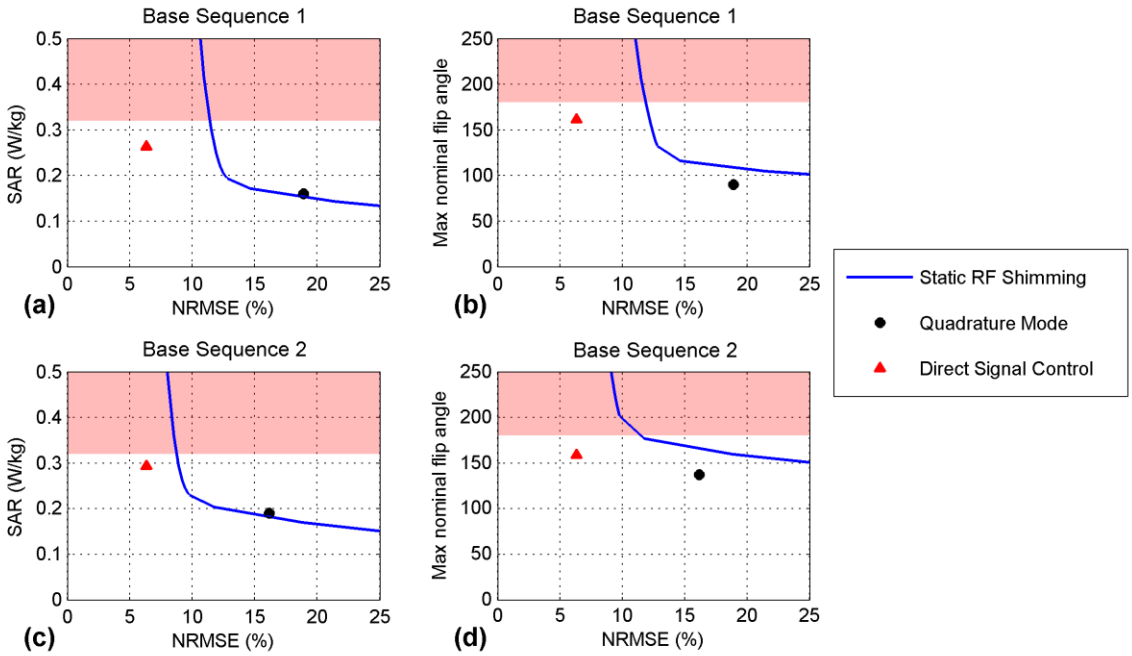

Figure 7 Simulated static shim experiments alongside quadrature and Direct Signal Control. NRMSE values are computed from the difference between a full transient simulation of the indicated solution and the ideal response of the base sequence. Solutions exceeding the SAR/peak power constraints are shaded. (a,c) Predicted SAR vs NRMSE; SAR is not allowed to exceed 0.32 W/kg (10% of the regulatory limit) (b,d) Maximum nominal flip angle vs NRMSE; regions with flip angle exceeding 180° violate the peak power constraint. Base sequence 2 contains higher flip angles at the start so is more restricted by both the maximum flip angle and SAR constraints.

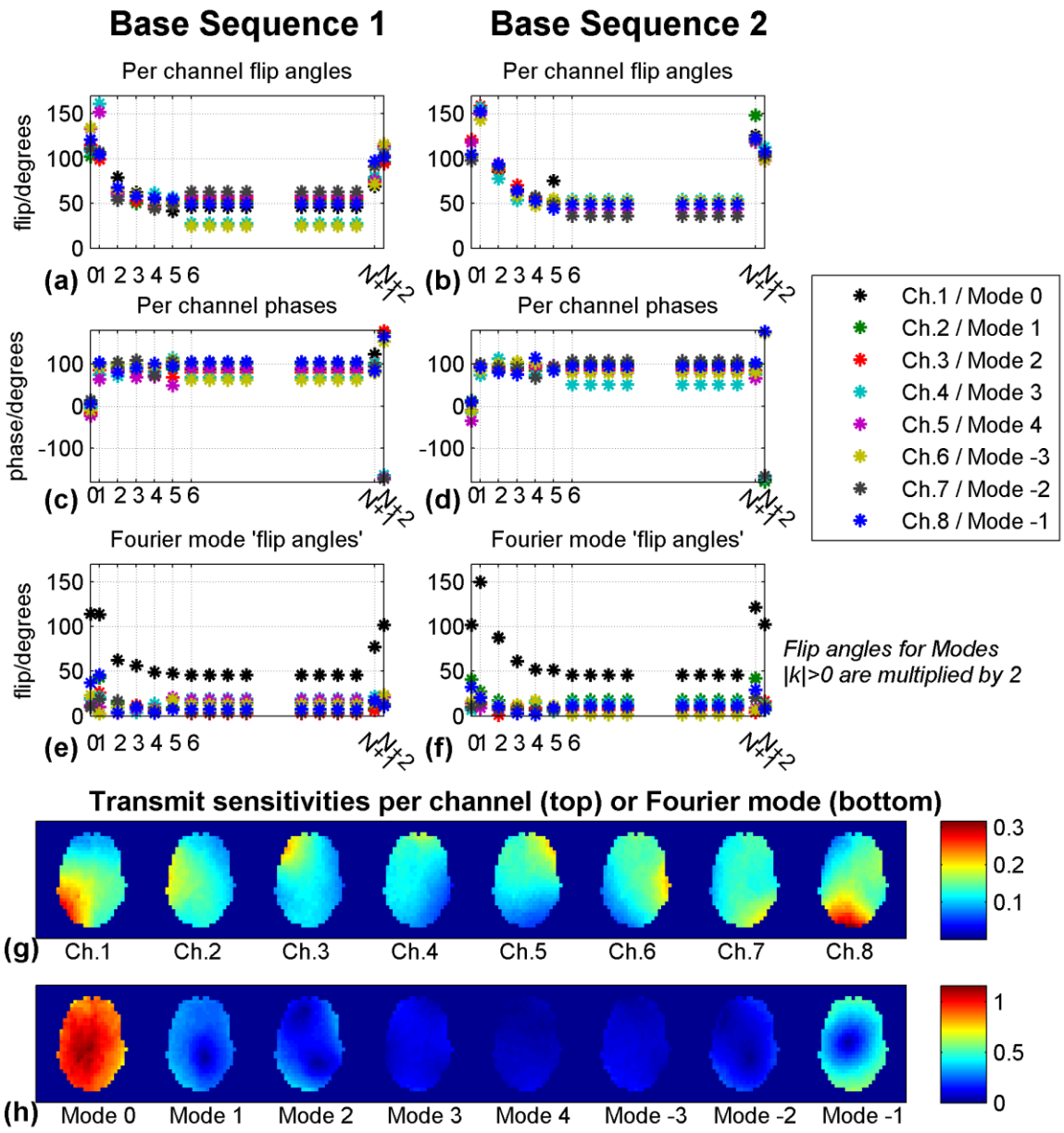

Figure 8 (a)-(d) DSC optimized pulse amplitudes and phases (A_{ij}) for both base sequences. The pulses are numbered from 0 to N+2 where 0 corresponds to the excitation and N+2 the flip back pulse. Note the approximately 90° phase difference between excitation and refocusing pulses on (c)&(d) required to maintain the CPMG condition – this is allowed to vary since echo instability is modeled by SR-EPG and penalized in the optimization. (e)-(f) Flip angles corresponding to a Fourier domain representation; flip angles for modes other than quadrature mode (k=0) are multiplied by 2 to aid visibility. (g) Transmit sensitivity of each channel ($\sigma(\mathbf{r})$ is a dimensionless quantity). (h) Transmit sensitivity of each Fourier mode (see text). The total flip angle for each pulse is the weighted sum over the channel sensitivities weighted by that channel's (complex) nominal flip angle, or equivalently the weighted sum over the Fourier modes weighted by that mode's (complex) nominal flip angle.

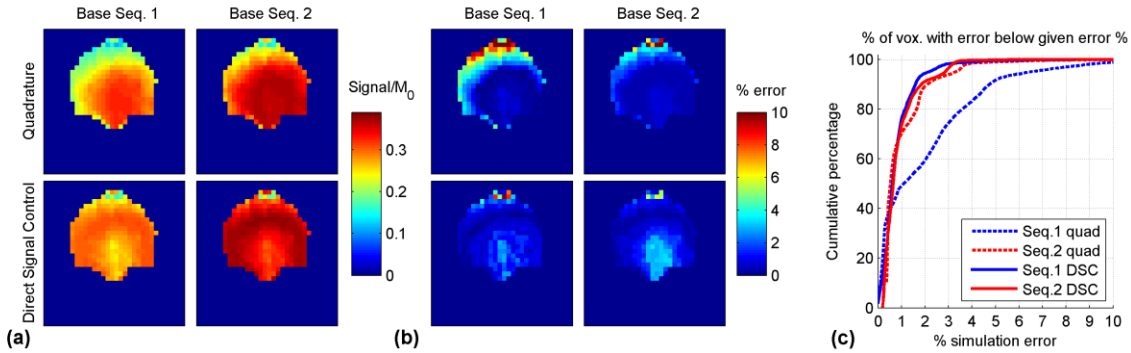

Figure 9 (a) Simulated echo amplitudes using *direct* method; these echo amplitudes are relevant to CSF so they are not direct predictions of image signal values obtained from a wide range of brain tissues. (b) Errors caused by using direct method with respect to full transient simulation. (c) Percentage of voxels in full 3D domain with simulation error below the given value. For example, for base sequence 1 in quadrature mode, only 76% of voxels have lower than 3% error whereas 94% of voxels meet this criterion for base sequence 2 in quadrature as do 97% and 98% for the respective base sequences after dynamic shimming.

Appendix: Efficient approximate EPG computation method for PSS sequences

Fig. A1 shows EPG diagrams for a PSS sequence yielding echo amplitudes of $0.5M_0$ neglecting relaxation. From Fig.A1(a) we see that as the train continues, the energy (i.e. states with high populations) is maintained largely in two sets of states: either close to the zero dephasing axis ('set 1') or on the leading diagonal of highly dephased states ('set 2'). Set 1 represents states that contribute to the PSS. It is a general property of PSS sequences that contributions are limited to mainly low order states, the most extreme example being 180° refocusing where all energy is kept in states with $k=\pm1$. Set 2 represents the half of the transverse magnetization that is initially created by the excitation pulse but does not contribute to echoes (echo amplitudes of $0.5M_0$ are used) and is further dephased as the sequence continues.

The structure of a generic CPMG FSE sequence means that some specific reductions in the number of necessary computations can be made, the most common being only computing populations of odd-numbered states since these alone contribute to the observed echoes (15). Additionally it was shown in ref.(11) that as a sequence goes on, an increasing number of higher order states cannot contribute to any echo, so may be dropped. These are illustrated on Fig.A1(b), and this may be done with no loss of accuracy. Further reductions are possible for certain types of FSE sequence, at the expense of a loss of generality and some errors. Since PSS sequences concentrate energy in low order states, a simple approach would be to only evaluate states below a specific order; Fig.A1(c) illustrates this for imposing a cutoff of $|k|\leq11$. Figs.A1(e)&(f) show that this rather aggressive strategy would result in oscillating errors greater than 2% for this sequence. The errors originate from the dephasing magnetization ('set 2') which is unable to propagate past the cutoff and so creates errors after the 7^{th} refocusing period that are refocused in subsequent periods and create observable errors from the 13^{th} echo. These errors have less of an impact if the simulation is run for more pulses before dropping to a lower limit of $|k'|$, as illustrated in Fig.A1(d). In this case the 'set 2' magnetization is concentrated in states with $k>k'$ so that when we limit to low order states, it will no longer contribute. Instead we focus on 'set 1' which has entered a PSS condition with more stable amplitudes. This method generates much lower error in observed echoes (<0.2% in the example above) for PSS sequences with echo amplitudes of $0.5M_0$ and higher, and has been used in this work with a cutoff of $|k|\leq11$ employed after 30 refocusing periods.

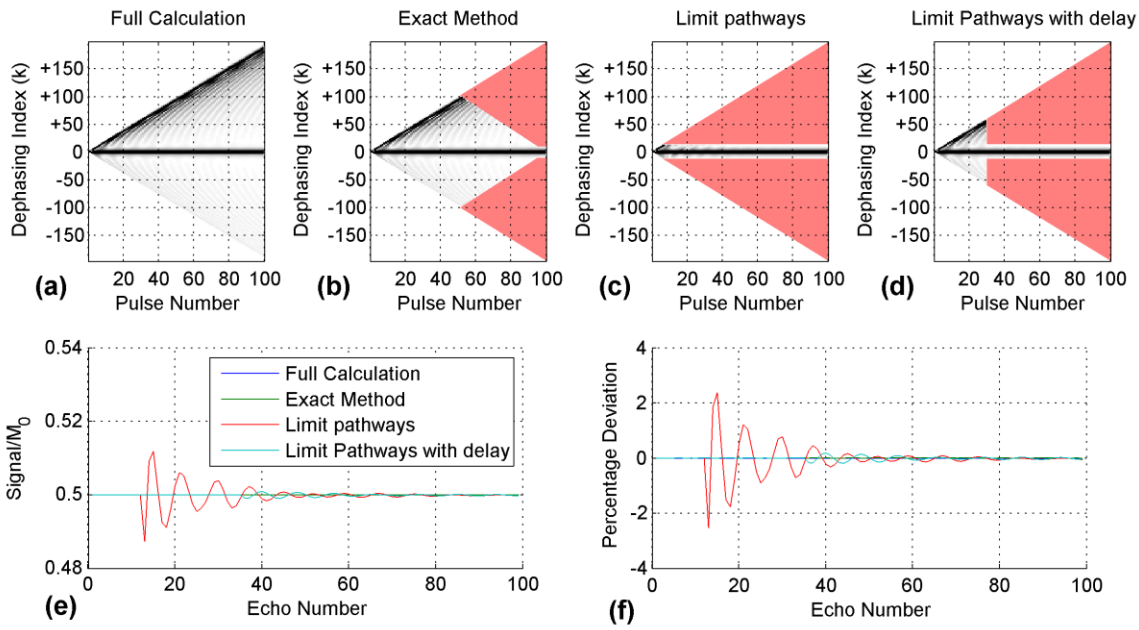

Figure A1 (a) Standard EPG calculation for a 100 echo PSS pulse train yielding echo amplitudes $0.5M_0$. Relaxation is ignored in this figure and phase graphs are plotted with a reversed gray scale where black indicates states with high populations. (b-d) Methods for reducing the number of states included in the calculation (details in text). Shaded states are excluded: the larger the shaded region the larger the reduction in required computational effort. (e) Echo amplitudes obtained by each method – all echoes should have amplitude $0.5M_0$. (f) Percentage error for each method.